Composites Part C: Open Access 17 (2025) 100597

Contents lists available at ScienceDirect

Composites Part C: Open Access

journal homepage: www.elsevier.com/locate/composites-part-c-open-access

Compression after impact behavior of flat and tapered Single-Double carbon composite specimens

Alessandro Vescovini [a,b,*], Carina Xiaochen Li [c], Bo Cheng Jin [d], Andrea Manes [a]

[a] Politecnico di Milano, Department of Mechanical Engineering, Milan, Italy
[b] German Aerospace Center, Institute of Lightweight Systems, Braunschweig, Germany
[c] University of Southern California, Department of Chemical Engineering and Materials Science, Los Angeles, CA, USA
[d] University of Southern California, Department of Aerospace and Mechanical Engineering, Los Angeles, CA, USA

ARTICLE INFO

Keywords:
Single-Double
Compression after impact
Thermography
Digital image correlation
Finite element analysis

ABSTRACT

This research investigates the damage tolerance with compression after impact (CAI) testing procedure of five sets of specimens, that were manufactured using the card-sliding technique with non-crimp fabrics (NCFs) and adopting a Single-Double (SD) stacking sequence. Before undergoing CAI tests, initial damage was generated in the specimens with low-velocity impacts. Two sets of specimens are flat with a constant cross-section and they are manufactured with ± 45° and ± 30° NCFs, respectively. Two sets feature a tapered cross-section and the same NCFs as the flat ones, and the fifth set consists of tapered specimens with the same fiber orientation as one of the tapered sets but feature NCFs with different areal density. The CAI tests were performed according to the ASTM standard, using an infra-red camera and a digital image correlation system to record the thermal transient and the displacement of the specimens. Finite Element Analyses are validated and compared with the experimental results. The failure modes are discussed focusing on the various damage mechanisms, highlighting the effect of the tapered cross-section, the different NCFs, and the stacking sequence. This research provided insights on NCFs composite damage tolerance after low-velocity impact damage, highlighting the effect of adopting the novel SD stacking sequence and card-sliding method to taper the laminate. The analysis underscores the possibility to develop composites mitigating delamination risks and promoting intra-laminar damage.

1. Introduction

The extensive use of composite materials across various sectors has highlighted the necessity of examining the damage tolerance of composite structures. Throughout the lifecycle of composite structures, impacts are not only possible but expected, potentially leading to damage that is difficult to detect and could compromise structural safety and reliability. Impact damage is the most critical type of damage among the ones that are not visually detectable, hence why they are often addressed as barely visible impact damage (BVID). Compression-after-impact is often used as a standard test to investigate the effect of BVIDs, in particular, damage tolerance measures the ability of a composite structure to bear a certain load without failing, after withstanding a specific damage extent [1–3].

Given the complexity of damage in composites subjected to Compression-After-Impact (CAI) testing, the mechanisms influencing the maximum CAI strength have gained significant attention in recent years. Sublaminate buckling is widely recognized as the primary cause of the abrupt reduction in strength observed during CAI testing, resulting in unstable propagation of delamination and leading to the ultimate collapse of the CAI specimen [4]. Wang et al. found that delamination initially propagates on the sides of the 0° layers, especially if located near the impact surface; also, they reported a little direct relationship between local buckling and delamination propagation as they occur in different regions and different loading stages, while underscoring the importance of geometrical imperfections [5]. Similarly, Yin and Iannucci highlighted the contribution of out-of-plane transverse deformation of sublaminates in promoting fiber compressive failure due to bending stress, which corresponds to the maximum CAI strength, followed by delamination propagation and sublaminate buckling [6].

In the scientific literature and most industry applications, composite structures are manufactured using a balanced symmetric stacking sequence of carbon fiber plies at 0°, 90°, and ± 45° angles, known as the quasi-isotropic stacking sequence (quad). However, recent research, supported by Prof. S. W. Tsai, has introduced an innovative layup

* Corresponding author.
E-mail address: alessandro.vescovini@dlr.de (A. Vescovini).

https://doi.org/10.1016/j.jcomc.2025.100597
Received 16 October 2024; Received in revised form 26 March 2025; Accepted 16 April 2025
Available online 27 April 2025

technique involving the repetition of four plies [±Φ/ ± Ψ] or two plies [±Φ] sub-laminates, named Double-Double (DD) or Single-Double (SD) stacking sequences, respectively [7,8]. This method simplifies the manufacturing process while allowing continuous selection of the repetitive unit's angle based on specific stiffness and strength requirements. Plies can be removed by eliminating one repetitive unit, avoiding negative impacts on in-plane stiffness or abrupt thickness changes. Converting the Quad composite stacking sequence to DD has shown potential for weight reduction without compromising strength, as it homogenizes inter-laminar stresses and minimizes angle differences between adjacent plies [9–12]. Kappel applied findings on buckling in DD laminates to the 'horse-shoe' use case, a standard in laminate optimization, demonstrating a 7.8% weight reduction in the DD panel compared to previous optimal solutions, highlighting DD's simplicity and efficiency [13,14]. Vescovini et al. tested single stringer specimens under compression until collapse, comparing constant section skins and hats with tapered sections. Tapered specimens showed higher maximum loads before the collapse, with FEM simulations indicating that tapering delays skin-stringer separation by promoting a larger damaged area before collapse [15]. Recent work by Kappel et al. compared the performance of quasi-isotropic and DD laminates following compression-after-impact testing, noting similar delaminated areas and residual strength but different delamination patterns [16]. In this work, the authors also addressed the effect of cross-section tapering, by performing impact on both tapered and flat surfaces and then CAI; they reported remarkable characteristics of the delamination pattern among the different specimen groups, concluding that further investigation is warranted to define the optimal location of ply-drops. Another work by Abdulhamid et al. presented CAI tests on tapered specimens with traditional quad stacking sequence subjected to CAI [17]. They reported complex failure mechanisms and intricate delamination and fiber failure patterns, as well as similar damage tolerance of tapered and flat laminates.

In recent years, non-crimp fabrics (NCFs) have emerged as a promising alternative to traditional unidirectional (UD) prepreg tapes and crimp textiles. NCFs, made of stitched UD thin plies, offer a simplified manufacturing process for DD composite design, with each fabric serving as half of the repetitive unit. While yarns in NCFs slightly reduce in-plane elastic and strength properties, particularly in thin plies, they still perform comparably to UD prepreg laminates. NCFs cater to the growing demand for enhanced damage resistance, out-of-plane properties, and cost-effectiveness [18–20].

This study aims to investigate the damage tolerance and damage mechanisms with CAI tests of Single-Double coupons manufactured with NCFs. NCFs with different orientations are used as repetitive units in both flat and tapered specimens. Given the simplified tapering process with this new stacking sequence, tapered coupons with fabrics of varying areal weights were produced to evaluate their effect on damage patterns. The effect of the SD stacking on the failure mode is discussed, and the analysis exploits results from an infra-red camera and digital image correlation. Numerical simulations were conducted, and specific features in failure mechanisms and damage patterns were analyzed. Section 2 presents the materials used and the specimen preparation procedures, including details of the low-velocity experimental campaign presented in a previous work [21]. In Sections 3 and 4 the experimental setup and procedure, as well as the numerical models used for finite element analyses are described, respectively. The results and discussion are presented in Section 5, and the conclusions are drawn in Section 6.

2. Single-double specimens manufacturing and low-velocity impact testing

Prior to carrying out the CAI testing procedure that this work focuses on, the specimens were manufactured, and low-velocity impact tests were performed. The results from that testing campaign have been presented in the work of Vescovini et al. and summarized in this Section [21].

2.1. Single-double specimens

The study utilized Chomarat's carbon NCF C-PLY^{TM} T700. The dry fabrics have an areal weight of 100 gsm or 600 gsm per bi-angle layer, with each single ply approximately half the weight per square meter. Three fabric types were used:

- NCF with +45° and −45° orientations and an areal weight of 100gsm (referred to as BX45-100) [22];
- NCF with +30° and −30° orientations and an areal weight of 100gsm (referred to as BX30-100) [23];
- NCF with +45° and −45° orientations and an areal weight of 600gsm (referred to as BX45-600) [24].

The fabrics were infused with epoxy resin using a vacuum infusion process and consolidated in an oven. The manufacturing was conducted out-of-autoclave (OoA), utilizing a low-viscosity epoxy resin/hardener matrix system (ProSet INF 114/212) [25]. Thirty specimens were prepared at the University of Southern California, divided into five sets of six specimens each. The sets included two control groups with constant thickness (Flat30 and Flat45 specimens) and three sets of tapered specimens (Taper30, Taper45, and Taper45-600 specimens). The tapered specimens with 100 gsm fabrics comprised 10 layers, each with 5 plies, with a taper interval offset. The 600 gsm specimens had two layers, also with 5 plies each. The taper width was 10.2 mm, with a taper ratio of 5:1 for all specimens. Flat specimens were designed to match the weight of the tapered ones by calculating the total surface area of all plies used in a tapered specimen and dividing it by the surface area of each ply of the control specimen. The manufacturing process for these tapered specimens leveraged the card-sliding technique [26], which offsets the layers according to the specified tapering strategy. The specimens utilized a non-symmetric balanced stacking sequence, allowing the tapering of the cross-section without abrupt thickness changes.

Fig. 1 illustrates the stacking sequence of the specimens, with black bars representing a NCF and arrows indicating the repetition of the sequence. The control specimens stacking sequence for Flat45 and Flat30 was defined as $[\pm 45_{30}]$ and $[\pm 30_{30}]$, respectively. For the tapered specimens, the stacking sequence for Taper45 and Taper30 can be defined as $[\pm 45_n]$ and $[\pm 30_n]$, respectively, where n ranged from 10 to 50; for Taper45-600 specimens, n ranged from 2 to 10.

Table 1 presents the average measurements of the specimens. Control specimens have a single average thickness value for both sets, while tapered specimen thickness variations are accounted for with average, minimum, and maximum values. The average density of the specimens was 1.45 g/mm^3, calculated for specimens with constant thickness. Fig. 2 shows the cross-section of flat and tapered specimens made from 100 gsm and 600 gsm fabrics.

2.2. Low-velocity impact testing

Low-velocity impacts were carried out on the Single-Double specimens using the StepLab DW1000 drop-tower, conforming to ASTM D7136 standards [27], with a 16 mm diameter hemispherical impactor. Impacts were centrally located on the specimens. The impact energies tested were 15.22 ± 0.04 J, 22.30 ± 0.09 J, 32.89 ± 0.16 J, and 39.86 ± 0.05 J, using an impactor mass of 5570.7 g. Two impacts were conducted at 15 J, 22 J, and 33 J, effectively simulating heavier tool drop [3]. However, tapered specimens were only impacted once at 15 J and once at 40 J, as visual inspection revealed relatively small damage at 33 J. Tapered specimens were impacted on the thickest part of the cross-section, with the flat side on the machine fixture. During the impact tests, passive infrared (IR) thermography was used to assess impact damage, with the thermal transient of the specimen's rear surface recorded by a FLIR X6900sc IR camera at 915.9 Hz. After impact, one specimen from each set tested at 33 J was sectioned along

Table 1
Specimens physical properties [21].

	Flat45	Flat30	Taper45	Taper30	Taper45-600
Weight [g]	73.92 ± 0.15	75.47 ± 0.07	75.59 ± 2.24	78.41 ± 5.73	73.58 ± 2.95
Avg. Length [mm]	151.7 ± 0.1	151.8 ± 0.1	151.8 ± 0.3	150.5 ± 2.5	151.3 ± 0.5
Avg. Width [mm]	101.0 ± 0.1	101.1 ± 0.0	100.2 ± 0.6	101.1 ± 2.5	100.3 ± 0.8
Avg. Thickness [mm]	3.33 ± 0.02	3.39 ± 0.01	3.22	3.27	2.97
Min. Thickness [mm]	–	–	1.37 ± 0.09	1.22 ± 0.31	1.11 ± 0.12
Max. Thickness [mm]	–	–	5.68 ± 0.17	5.74 ± 0.42	5.23 ± 0.09

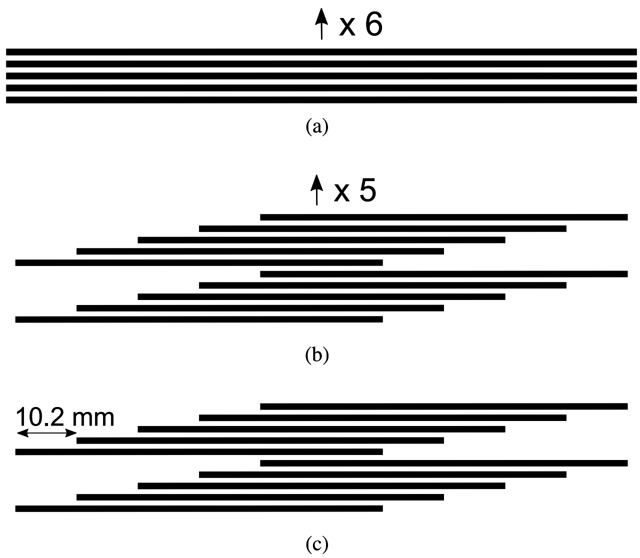

Fig. 1. Stacking sequence schematic representation of (a) the flat specimens, (b) the tapered specimens, and (c) the tapered specimens manufactured with 600 gsm fabrics [21].

Fig. 2. Cross-section cut of (a) the Flat45 specimen, (b) the Taper45 specimen and (c) the Taper45-600 specimen [21].

the plane parallel to the short edge using an automatic diamond saw, hence the number of specimens that was subjected to the compression after impact procedure was 25.

The results of the low-velocity impacts are summarized in Table 2 and in Table 3 the average stiffness is reported for each specimen type.

In Fig. 3 few impact damage pictures are reported from the low-velocity testing campaign, highlighting the damage in the specimens with red dashed lines. These pictures were taken with an optical camera and then resized to maintain the proportions of the specimen and magnify the extent of damage. In Fig. 3(a) cracks induced by compressive and tensile stresses on the impact and back sides are visible, respectively, aligned with the fiber directions of the NCFs, while for the tapered specimen in Fig. 3(b), there are larger cracks on the impact side than on the back side. For the Taper45-600 specimen in Fig. 3(c), the residual indentation is visible on the impact side, but cracks oriented along the fiber directions are barely noted; on the other hand, matrix cracks are instead reported along the ply drops and highlighted

Table 2
Summary of the impact results [21].

Specimens		Maximum Force [kN]	Maximum Displacement [mm]	Norm. Abs. Energy [J/J]
Flat45	15 J	4.45 ± 0.04	5.35 ± 0.04	0.74 ± 0.01
	22 J	4.86 ± 0.17	6.99 ± 0.16	0.80 ± 0.08
	33 J	4.94 ± 0.07	10.16 ± 0.00	0.95 ± 0.00
Flat30	15 J	4.75 ± 0.10	5.49 ± 0.03	0.70 ± 0.01
	22 J	5.13 ± 0.01	7.08 ± 0.24	0.80 ± 0.09
	33 J	5.25 ± 0.38	10.66 ± 0.66	0.95 ± 0.01
Taper45	15 J	6.53	3.89	0.66
	22 J	7.20 ± 0.40	4.78 ± 0.18	0.68 ± 0.03
	33 J	7.88 ± 0.07	6.13 ± 0.15	0.74 ± 0.01
	40 J	7.96	6.75	0.79
Taper30	15 J	4.60	4.91	0.82
	22 J	6.71 ± 0.05	4.92 ± 0.04	0.70 ± 0.01
	33 J	7.23 ± 1.10	6.92 ± 0.86	0.74 ± 0.07
	40 J	8.75	6.84	0.69
Taper45-600	15 J	4.47	4.96	0.86
	22 J	5.75 ± 0.71	5.89 ± 0.47	0.78 ± 0.02
	33 J	6.47 ± 0.47	7.49 ± 0.57	0.79 ± 0.02
	40 J	5.64	9.80	0.88

Table 3
Average impact stiffness [kN/mm] [21].

Flat45	Flat30	
1.22 ± 0.03	1.04 ± 0.03	
Taper45	Taper30	Taper45-600
2.27 ± 0.12	2.20 ± 0.16	2.08 ± 0.12

with red dashed lines on the back side, and no fiber failure is observed at the impact location (highlighted with transparent white circles for reference).

In Fig. 4 the IR camera pictures are reported from the low-velocity testing campaign, underscoring the damage in the specimens. In particular, in Fig. 4(a) and 4(b) after 2.2 ms, i.e., approximately at the impact force peak, an abrupt temperature increase indicated the fiber failure then coalescing after 895.3 m. In Fig. 4(c) different damage mechanisms are highlighted by the IR camera: delamination and matrix cracking are the main mechanisms for the Taper45-600 due to the different fabrics employed for these specimens. The heavier and thicker layers affect laminate homogenization and result in bigger resin pockets in the laminate outer surface, rendering the laminate prone to delamination. The interested reader is referred to the work discussing these results for further insights on the low-velocity experimental campaign [21].

3. Experimental setup

The Single-Double specimens underwent CAI testing on MTS Alliance RF/150 testing machine. The testing procedure was based on the ASTM D7137 standard [28]. The standard testing fixture was used according to the standard specifications, the bottom end was fixed while the top applied the compression load. The load cell in the crosshead acquired load data at 20 Hz. Once the specimen was placed in the testing fixture, two load cycles were carried reaching 250 and 450 *N*

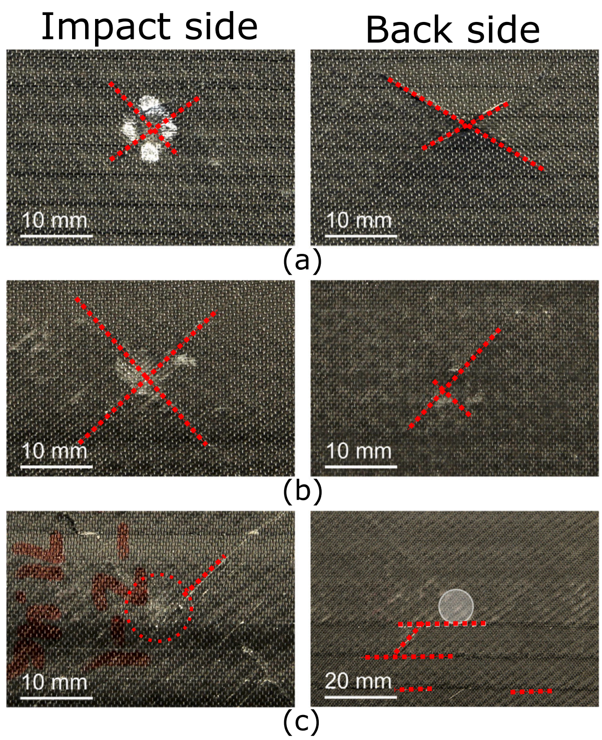

Fig. 3. Impact and back sides views of (a) the Flat30, (b) the Taper45 and (c) the Taper45-600 specimens tested at 33 J [21].

and unloading to 150 N; finally, the test was run until specimen failure with a crosshead displacement rate of 1.25 mm/min, as suggested by the standard.

To measure the crosshead displacement accounting for possible machine compliance, a deflectometer was installed with the deflecting tip positioned on the CAI fixture top plate. To assess the damage during the CAI test, passive infrared (IR) thermography was adopted. The specimen rear surface thermal transient is recorded with the IR camera FLIR X6900sc, having an Indium Antimonide (InSb) detector and a Noise Equivalent Temperature Difference (NETD) smaller than 20 mK. The acquisition frequency is 2 Hz with a 640 x 512 frame resolution. The data acquired by the IR camera are post-processed with a Python script. The image is normalized as $\Delta T = T_i - T_0$; where T represents thermal matrices, i represents the i^{th} frame of the recording, and 0 refers to the frame recorded before the test start. The Aramis Gom DIC system captured the displacement of the impact side of the specimen, with the same acquisition frequency as the IR camera. The experimental setup is depicted in Fig. 5.

After the tests, pictures of the failed specimens were taken with a commercial optical camera. Then a few specimens were cut with an automatic diamond saw blade in positions where cracks resulted from the compressive load, and were far from the pre-existing impact damage, along the plane parallel to the longer edge. Pictures of the cut face are taken with a Zeiss SteREO Discovery V12 stereomicroscope, to observe the microscopic features of the cracks.

4. Finite element analysis

The finite element analyses (FEA) employed the Abaqus 2023 “Quasi-Static” Dynamic Implicit solver with automatic time stepping [29]. To perform the CAI analyses, the FEM model was previously built and low-velocity impact simulations were carried out; the results of these simulations are presented in the previous work [21]. Then after the LVI analysis was completed, the same model was used and the results in terms of damage variables were imported from the preceding

Table 4
Engineering properties, ply strength, fracture toughness, and interlaminar strength and properties of the carbon composite material [19,32,33].

Property	Value	Property	Value	Property	Value
E_1 [GPa]	110	X_T [MPa]	2300	G_{Ic} [N/mm]	0.28
E_2 [GPa]	7.4	X_C [MPa]	1500	G_{IIc} [N/mm]	0.69
ν_{12} [ ]	0.3	Y_T [MPa]	66	σ_{zz} [MPa]	43
G_{12} [GPa]	4.2	Y_C [MPa]	93	σ_{xz} [MPa]	66
				η [ ]	1.5

impact analyses as an “initial state” of the simulation. The geometry was updated from the previous simulation, i.e., no residual stress or acceleration (as well as velocity and displacement) are imported from the previous analysis.

The specimens were modeled using 8-node quadrilateral continuum shells (SC8R), featuring a 1 mm characteristic size in a 30 × 30 mm region around the impact area, transitioning to a 2 mm size in the constrained part of the specimen. For the flat specimen, six layers of continuum shell elements were used through the thickness, while the tapered specimen had one layer for the thinnest section and five layers for the thickest, dropping one layer of elements with each ply drop. Between each layer of elements, a zero-thickness three-dimensional cohesive element (COH3D8) layer was modeled. The composite stacking sequence was defined using the Abaqus “Composite Layup” tool, with each unidirectional (UD) ply within the non-crimp fabric (NCF) specified in the layup and assigned three integration points. This approach generated unique stacking sequences for each finite element layer based on its position within the models. The model uses the Abaqus Hashin failure criteria [30], to monitor intralaminar damage within the composites, applying a linear softening law for progressive damage simulation. The interlaminar behavior follows the cohesive zone model, with damage initiation governed by the Abaqus quadratic nominal stress criterion and damage evolution governed by the Benzeggagh-Kenane fracture criterion, which allows cohesive element properties to degrade linearly after damage initiation [31].

Simply supported boundary conditions are applied to both sides of the specimen in correspondence with the CAI fixture slide-plates. At the specimen ends, one edge is fixed, while the other is limited in all degrees of freedom except the one the end shortening is applied. Fig. 6 illustrates the finite element model of the flat specimen, highlighting the boundary conditions.

Material properties are sourced from existing literature and reported in Table 4 for the composite material.

After carrying out the low-velocity impact experimental tests [21], a discrepancy was noted between the stiffness of the specimens and that of the numerical simulation; it was then decided to resort to the analytical model proposed by Olsson [34,35], and exploit that series of tests to calibrate the stiffness of the specimens tested. The analytical model was based on a simplified two-mass structural dynamic model, and computes forces using the following equation:

$$F = \left(\frac{1}{k_b} + \frac{1}{k_s}\right)^{-1} w_p + k_m w_p^3 \tag{1}$$

In Eq. (1), w_p represents the specimen’s vertical displacement, and k_i are the contributors the specimens stiffness; in particular: k_b, k_s, and k_m denote bending, shear, and membrane stiffness, respectively. An iterative approach was employed to minimize the squared error $\left(\Sigma\left(x_{exp} - x_{an}\right)^2/n\right)$ between the experimental and analytical curves over the elastic displacement range.

The optimized parameter was the longitudinal modulus since it is the main responsible for the specimen stiffness; once the modulus was obtained from this approach, the longitudinal tensile and compression strength were scaled accordingly. The longitudinal toughness parameters required by the Abaqus built-in material model, are reduced to approximate an instantaneous failure for the fiber modes. The same

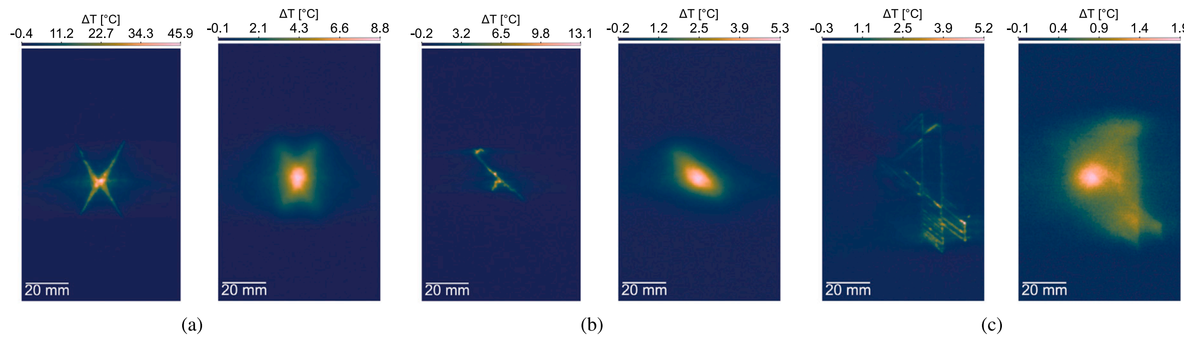

Fig. 4. IR camera pictures of (a) the Flat30, (b) the Taper45 and (c) the Taper45-600 specimens tested at 33 J obtained approximately 2.2 ms (left) and 895.3 ms (right) after the impact start [21].

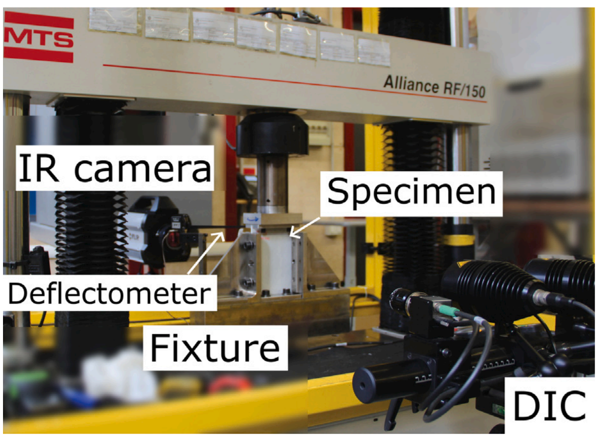

Fig. 5. CAI test set-up.

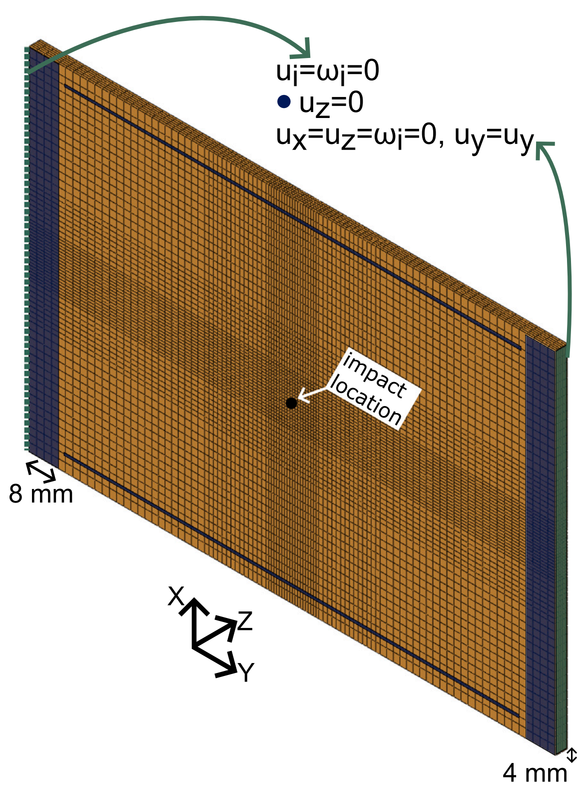

Fig. 6. FEM model (the same boundary condition is applied on both specimen surfaces).

Table 5
Summary of the CAI results.

Specimens		Maximum Force [kN]	Displacement at max. force [mm]
Flat45	15 J	45.44 ± 1.62	3.97 ± 0.30
	22 J	37.44 ± 2.19	3.83 ± 0.31
	33 J	32.03	2.25
Flat30	15 J	55.52 ± 5.15	0.93 ± 0.01
	22 J	53.43 ± 0.26	0.89 ± 0.01
	33 J	49.66	0.87
Taper45	15 J	34.73	3.70
	22 J	35.5 ± 0.67	3.99 ± 0.21
	33 J	30.20	1.86
	40 J	26.54	1.95
Taper30	15 J	24.23	1.11
	22 J	35.28 ± 0.87	1.89 ± 0.08
Taper45-600	15 J	25.09	1.33
	22 J	23.52 ± 4.24	1.17 ± 0.51
	33 J	23.03	1.32
	40 J	13.64	0.92

material properties used for the low-velocity impact simulations were considered for the compression-after-impact simulations described in this Section. The calibration was performed on the flat specimens constituted by BX45-100 fabrics, and resulted in an average longitudinal modulus of 81.9 GPa. Following this optimization, longitudinal tensile and compression strengths were adjusted proportionally based on the newly estimated fiber volume content to 1711 MPa and 1116 MPa, respectively, according to the mixture rule. Adjustments to longitudinal toughness parameters in Abaqus material model approximate instantaneous failure for the fiber modes, assuming 17.9 N/mm and 7.6 N/mm for the longitudinal tensile and compressive fracture toughness. These hypotheses are deemed acceptable, considering that the primary objective of this study is to investigate the behavior and the failure mode of specimens manufactured with the single-double stacking sequence.

5. Results and discussion

5.1. Experimental force–displacement curves

The experimental load–displacement curves for the CAI tests on the flat and tapered specimens are presented in Fig. 7 [36]. In Table 5 the experimental results are summarized and in Table 6 the average stiffness is reported for each specimen type. It is pointed out that for the Taper30 set, two specimens that were previously impacted at 33 J and 40 J failed near the edge of the specimens, and it was decided not to show these as the failure mode is deemed not acceptable by the standard.

Regarding the stiffness of the two flat specimens, the specimens with fibers oriented along the ± 30° are stiffer, as expected; while for the

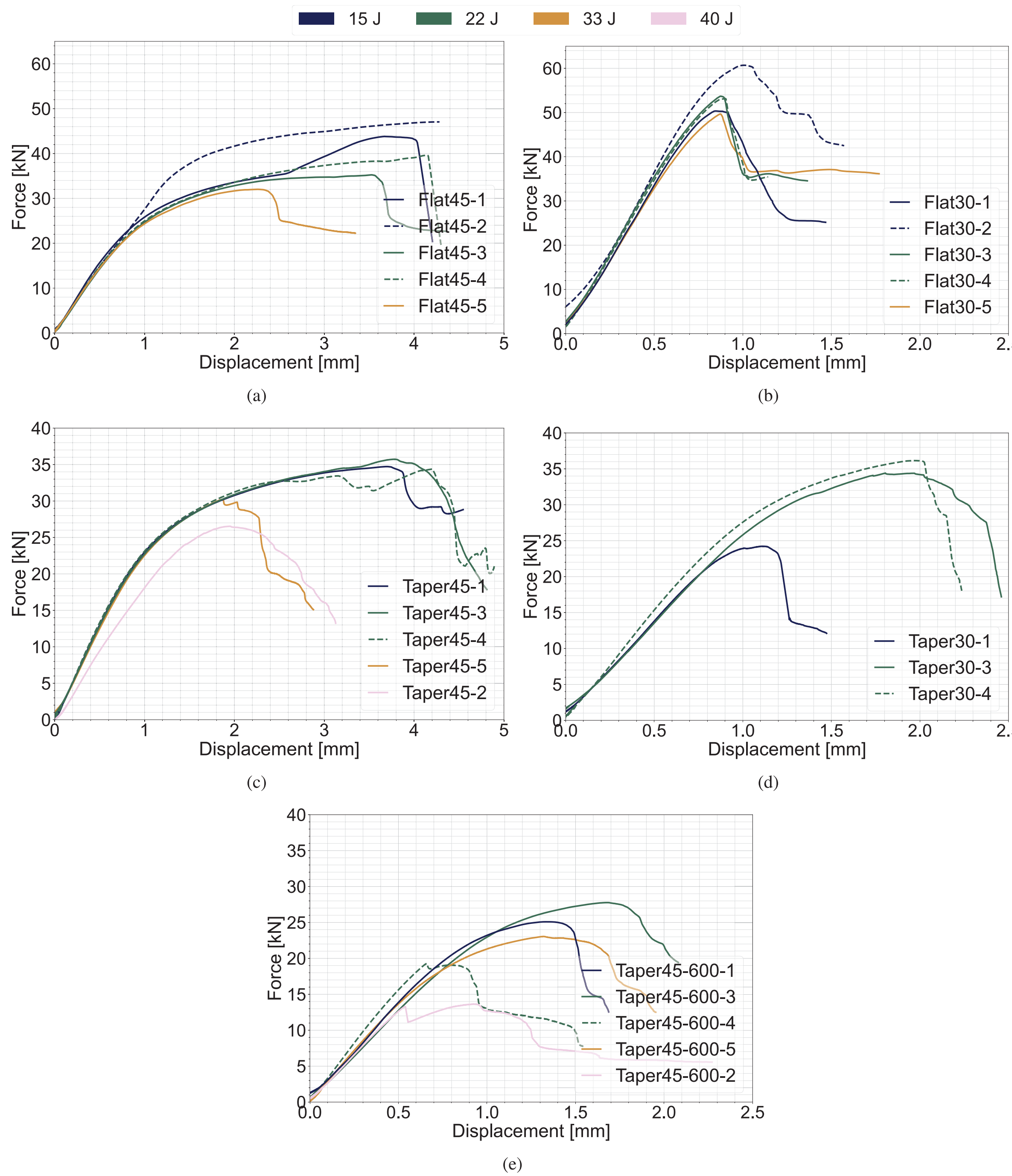

Fig. 7. Load vs. displacement curves of (a) the Flat45, (b) the Flat30, (c) the Taper45, (d) the Taper30 and (e) the Taper45-600 specimens.

Table 6
Average CAI stiffness [kN/mm].

Flat45	Flat30	
29.70 ± 2.74	69.37 ± 2.74	
Taper45	Taper30	Taper45-600
24.37 ± 2.92	28.62 ± 1.47	27.29 ± 2.44

tapered specimens, the difference between the stiffness of the ± 30° and the ± 45° specimens is significantly smaller, probably due to the tapered cross-section, and the stiffness varies more within the same group due to the variability in the cross-section thickness (Table 1). The Flat45 and Flat30 sets of flat specimens have different behaviors. In particular, for the former the force increases linearly up to 25 kN, except for the Flat45-2 specimen which reaches approximately 35 kN, then the specimen buckles globally resulting in the stiffness reduction until failure is reached; the Flat30 specimens instead show linear force–displacement behavior until maximum force is reached. This aspect also affects the displacement at maximum force, in fact, the Flat45 specimens reach a significantly larger maximum displacement. A similar pattern is reported for the Tapered specimens, the Taper45 stiffness reduces at 20 kN, earlier than the Taper30 set, reaching maximum force at larger displacement. This will be further addressed in Section 5.5 where the results from the DIC camera will be discussed. Due to the significantly different damage pattern of the Taper45-600 specimens, reported in Section 2.2, the CAI results of these specimens differ from those specimens manufactured with fibers aligned along the same direction but have fabrics with different areal densities. The Taper45-600 specimens have comparable stiffness to the Taper45 set but fail at significantly lower displacement and force.

Overall the maximum force decreases as the impact energy increases, and few exceptions are reported, such as for the Taper30 set where the specimens impacted at 22 J fail at a larger maximum force than those impacted at 15 J. Also, for the Flat30 and Taper45-600 specimens tested at 15 J and 22 J, respectively, the maximum force (and the displacement at maximum force) are quite scattered, with the lower bound failing at lower maximum force than the specimens impacted at higher impact energy.

5.2. Macroscopic observation

The views of the back sides of the Flat45-5 and Flat30-5 specimens are reported in Fig. 8(a) and 8(b), respectively. These two pictures are representative of the failure mode of the specimens belonging to these sets. Despite the different displacements at maximum force, the failure mode of these specimens is very similar. In both pictures, the square with white dashed lines indicates the area where the impact damage was visible before starting the CAI test. In the pictures, the surface cracks, that is visible on both surfaces of the specimens, propagated along the fiber direction starting from the impact crack tips, leading to the specimen failure [37].

In Fig. 9(a) and 9(b) the impact and back side views of the Taper45-5 specimen are shown. As a result of the low-velocity impact, the tapered specimens had larger damage extension on the impact side than on the back side, which is highlighted with white and black dashed lines in the pictures. After the CAI test, fracture originating from the damaged area propagate as visible from Fig. 9(a) and indicated by red arrows; in this case, as well as in other tapered specimens, they do not follow a straight path but tend to "zig-zag" along the fiber directions. On the back side of the specimen in Fig. 9(b), the fracture is barely visible and it is highlighted with red-dashed line, underscoring the different appearance of the damage in the two surfaces, unlike with flat specimens. In Fig. 9(c) the damage observed for the Taper30-5 specimen is presented, and the red arrows indicate the fracture that propagated from the area previously damaged by the LVI; the crack propagates along a fiber direction and changes direction close to the edge of the specimens, more similarly to the flat specimens shown in Fig. 8.

In Fig. 10 the impact and back side views of the Taper45-600-5 specimen are shown. The damage in the impact side in Fig. 10(a) is similar to that of the specimen Taper45-5 shown in Fig. 9(a); where large impact damage is marked by black dashed lines and the fracture resulting by the CAI test are indicated by red arrows. However, the damage in the back side in Fig. 10(b) is very different from that of the Taper45-5 specimen, underscoring the effect of the fabric with different areal density on the damage mechanism and failure. This set of specimens experienced severe delamination located at the ply drop as a result of the low-velocity impact due to bigger resin pockets and poorer homogenization in the composite, as presented in Fig. 4(c); the delaminated composite layers buckled locally in the back side of the specimen without leading visible crack on the back side.

5.3. Cross-section microscopic observation

To investigate further the damage and the fracture through the thickness in the CAI specimens, three specimens were cut along a plane parallel to the long edge far from the pre-existing impact damage. Two cross-section cuts are shown for the Flat30-5 specimen in Fig. 11, the pictures show fracture and cracks across the specimen thickness that have started propagating from the specimen back side (with large impact damage) and then grown to the specimen impact side. It is interesting to notice that on the impact side, few composite layers are not cracked but buckled as a result of the compressive

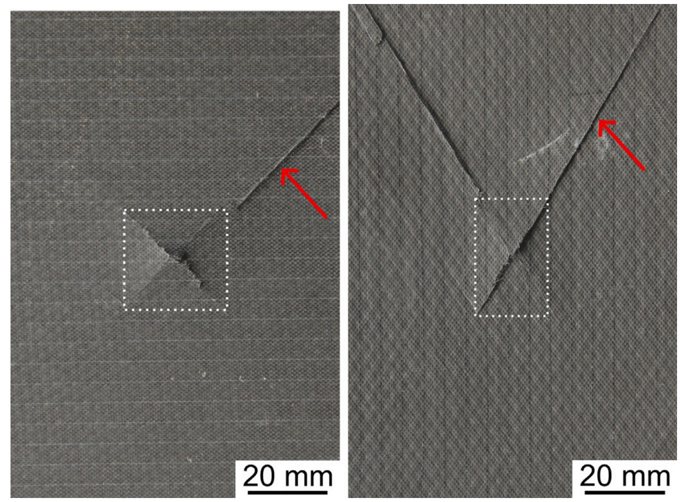

(a) (b)

Fig. 8. Back sides views of (a) Flat30-5 and (b) Flat45-5 specimens.

load; these layers are likely to contribute to the compressive force plateau reached after the maximum force and would have probably failed too if the test had been run up to larger vertical displacement. In addition, delamination had occurred in a plane offset from the specimen middle plane, and in the left picture, it is shown that the split between two adjacent layers caused the deviation of the fracture spanning through the thickness. The delamination propagated for a few millimeters along the *y*-direction. The cross-section cuts of Taper45 in Fig. 12 show a fracture that does not span through the whole thickness of the specimen. The same difference is found in the cross-section cut of the Taper45-600 specimen in Fig. 13. The fracture starts on the impact surface for these two specimens, then propagates through the thickness similarly to the flat specimen, and finally stops, propagating instead along a delamination plane. This difference in the fracture and cracks through the thickness remarks also the difference in the damage appearance described previously in Section 5.2, where the damage in the tapered specimens differed between the impact and back surfaces. It is worth noting that in the right cross-section of Fig. 13, diffused delamination is observed through the thickness, highlighting poorer laminate homogenization and a weaker interface between the laminae compared to the laminate with thinner fabrics, which affect composite properties and performance. The orientation of the fracture propagating through the thickness was consistent among the specimens presented and had approximately a 50° angle confirming the observations made in the literature about the fracture plane orientation in composite materials [38].

5.4. Passive thermography results

Passive thermography was used to monitor the thermal transient during the CAI test. The IR camera was pointed at the back surface of the specimens, hence the surface where the composite specimens were damaged due to tensile stress and fiber breakage due to the low-velocity impacts. Fig. 14 shows three pictures recorded by the IR camera before, before, after and at the maximum force measured during the test. In Fig. 14(a) it is visible that, as the specimen was reaching the maximum force, the ΔT was the highest around the pre-existing impact damage. Then at maximum force in Fig. 14(b) a sharper but still low increase of the temperature along the direction of the fibers highlighted the moment when the cracks were starting to propagate towards the specimen edge, leading to failure. Finally in Fig. 14(c) the large ΔT underscored the specimen failure, caused by the compression

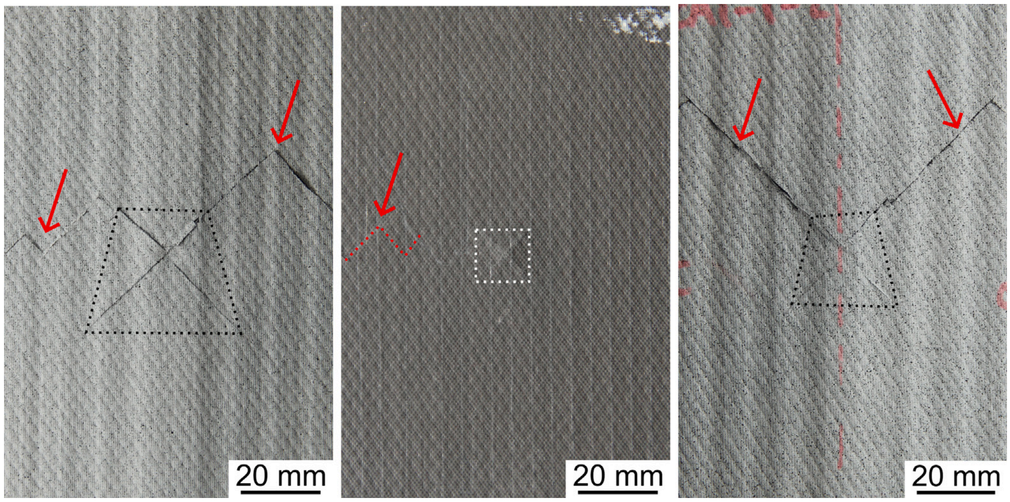

Fig. 9. (a) impact and (b) back sides views of Taper45-5 specimen and (c) impact side view of Taper30-4 specimen.

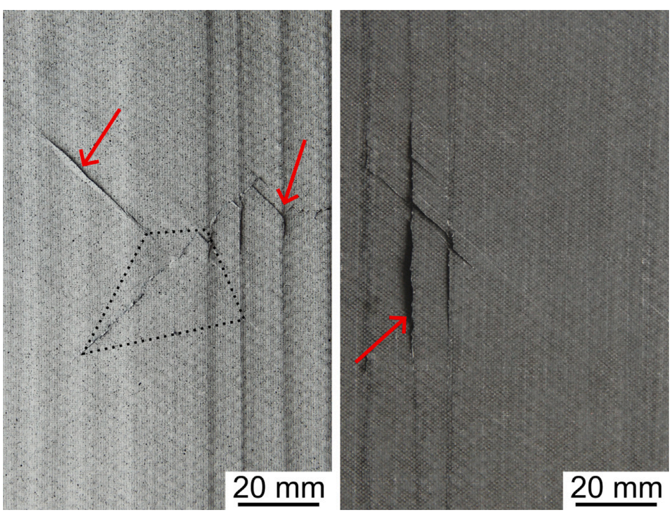

Fig. 10. (a) impact and (b) back sides views of Taper45-600-5 specimen.

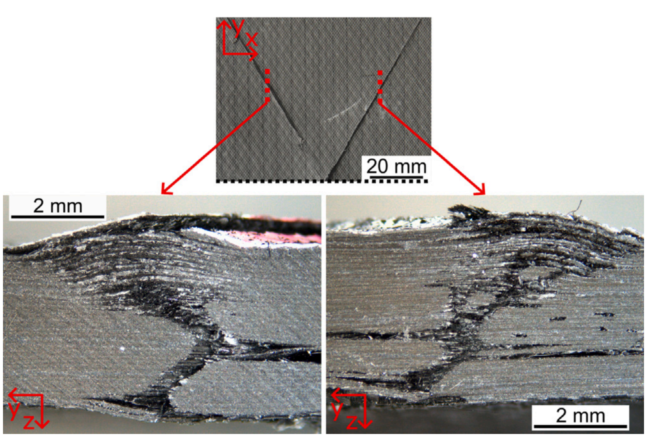

Fig. 11. Cross-section views of the Flat30-5 specimen.

shear load leading to the fracture along the direction of the fibers, as previously pointed out for Fig. 8(a).

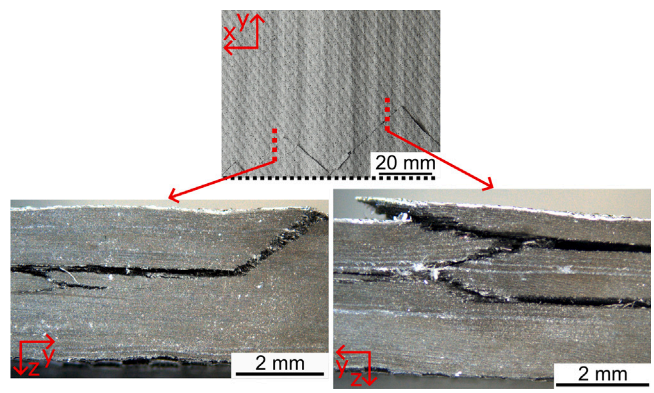

Fig. 12. Cross-section views of the Taper45-5 specimen.

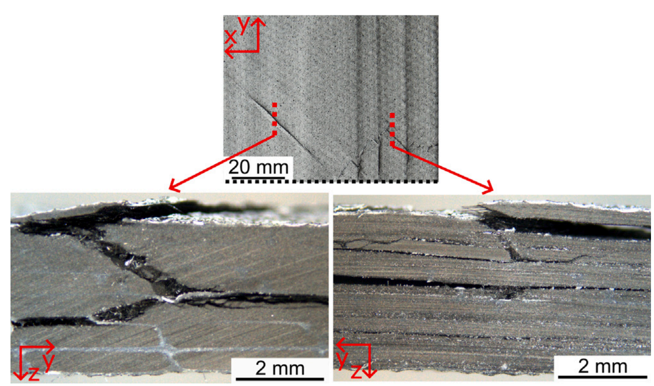

Fig. 13. Cross-section views of the Taper45-600-5 specimen.

Fig. 15 shows two pictures recorded by the IR camera after the maximum force was reached for CAI test of the Flat45-5 specimen. As previously discussed in Fig. 8, the two sets of flat specimens showed similar failure modes, with cracks running diagonally along the fiber orientation. Fig. 8(a) shows a sharp ΔT increase caused by the propagating crack, then coalescing over a larger area, as well as starting to appear on the left-hand side of the specimen with the force decreasing in Fig. 8(b).

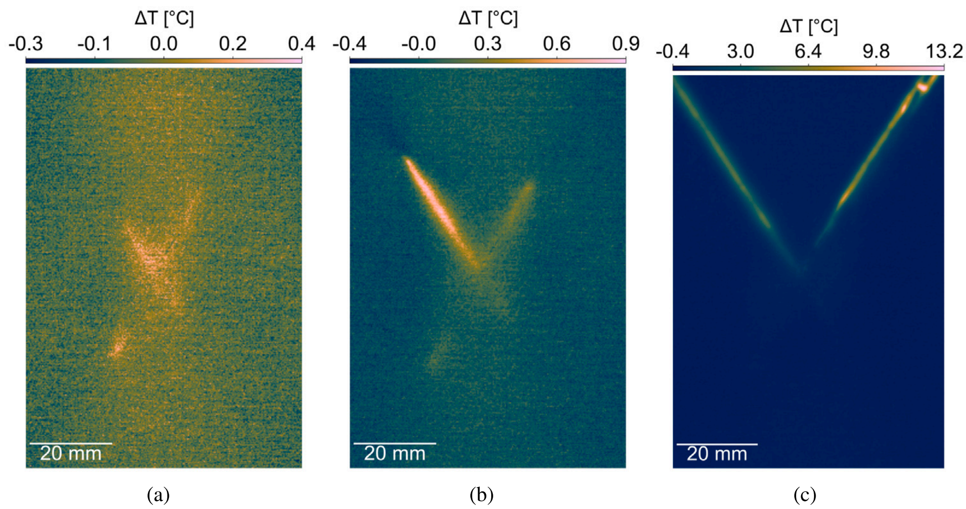

Fig. 14. IR camera pictures of the Flat30-4 specimen obtained approximately at (a) 50 kN (before max. force), (b) 53 kN (max. force), and (c) 45 kN (after maximum force).

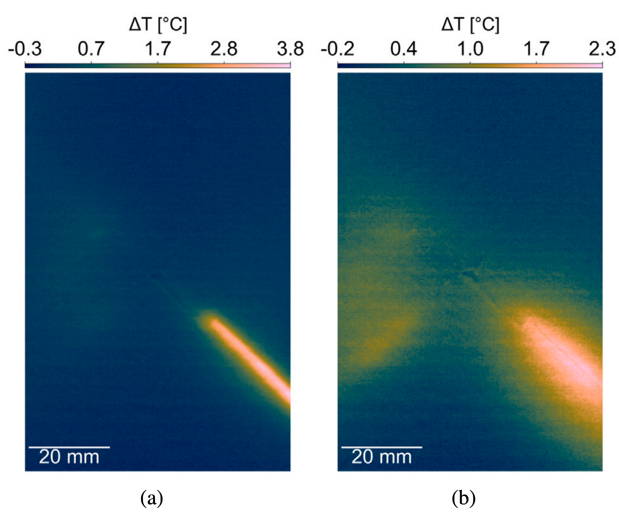

Fig. 15. IR camera pictures of the Flat45-5 specimen obtained approximately at (a) 25 kN and (b) 22 kN (after maximum force).

The thermal transient recorded during the CAI test of Taper45-5 is reported in Fig. 16. In Fig. 16(a), i.e., shortly before the first force drop, the damage coalesced around the pre-existing damaged area and along the direction of propagation of the crack, characterized by a small increase of ΔT. Then in Fig. 16(b) a crack propagates on the right-hand side of the specimen (as previously noted in Fig. 9(a), causing the drop of the compression force. Finally, in Fig. 16(c), as the force continued dropping the crack reached the left-hand side of the specimen and damage coalesced around the middle plane of the specimen (transversely to the loading direction).

A similar failure mechanism is reported for the Taper30-4 specimen, as shown in Fig. 17. Despite not showing a plateau in the force–displacement curve, once the maximum force is reached damage coalesces along the fiber direction as visible in Fig. 17(a), leading to the fractures that were previously reported in Fig. 9(c). After the loss of load-bearing capability due to the fractures, the force further drops and the damage appears around the middle plane of the specimen, as noticed by the increase of ΔT in Fig. 17(b), similarly to the Taper45-5 specimen.

The pictures from the thermal transient recorded during the CAI test of the Taper45-600-5 are presented in Fig. 18. Shortly after the maximum load is reached, damage starts from the impact location and propagates along the fibers direction, leading to fracture and failure. As this set of specimens experienced severe delamination at the ply drops as the result of the low-velocity impact, the damaged area marked by the increase of ΔT starts underneath the delaminated layers and continues until the edge of the specimen, not affecting the outer layer that faces the IR camera. After that a transverse crack (with respect to the loading direction) appears on the other side of the specimen, in this case offset from the specimen center. These two damage mechanisms are visible also from the optical camera picture, as shown in Fig. 10, however, the IR camera allows to define which mechanism leads first to the loss of load-bearing capability and at what stage of the load–displacement curve the different mechanisms occur.

5.5. DIC results

The DIC contour pictures of the major strain component are shown for the Flat30-5 and Taper45-5 in Fig. 19. The pictures are captured at the maximum force, before the force drops and fracture appears in the specimen, and they are representative of the strain contour measured by the DIC at the maximum force for the specimens manufactured with [± 30] and [± 45] fabrics, disregarding the different cross-section of the specimens. This underscores that fractures generated along the fibers direction are responsible for the loss of load-bearing capability of the specimens; after which other damage features can appear, as discussed in the previous Sections 5.2 and 5.4.

The DIC recordings were used to assess global buckling during the CAI tests. Buckling should be generally avoided when performing CAI tests, however, it is often facilitated by the residual indentation, the intra- and inter-laminar damage of the impacted specimen, especially after impact at high energy. Fig. 20 reported the out-of-plane displacement at the center for the specimens impacted at 33 J belonging to the five sets, as a function of the compressive load. Regarding the two Flat specimens, these showed similar behavior and reached a few millimeters of out-of-plane displacement at the maximum compressive force; because of the lack of carbon fibers aligned along the loading direction the bending stiffness was not enough to avoid this phenomenon. From the two curves shown for the flat specimens, it can be concluded that the Flat30 and Flat45 buckled approximately at 30 kN and 20 kN, respectively; however, it is hard to identify the exact transition point. A significantly different behavior resulted from the tapered specimens manufactured with 100 gsm fabrics: both Taper30 and Taper45 specimens showed small out-of-plane displacement within 1 mm until the maximum force, hence the stress can be reasonably approximated to be in the specimen plane, then increased due to specimens failure. For these two specimens, the thicker center of the

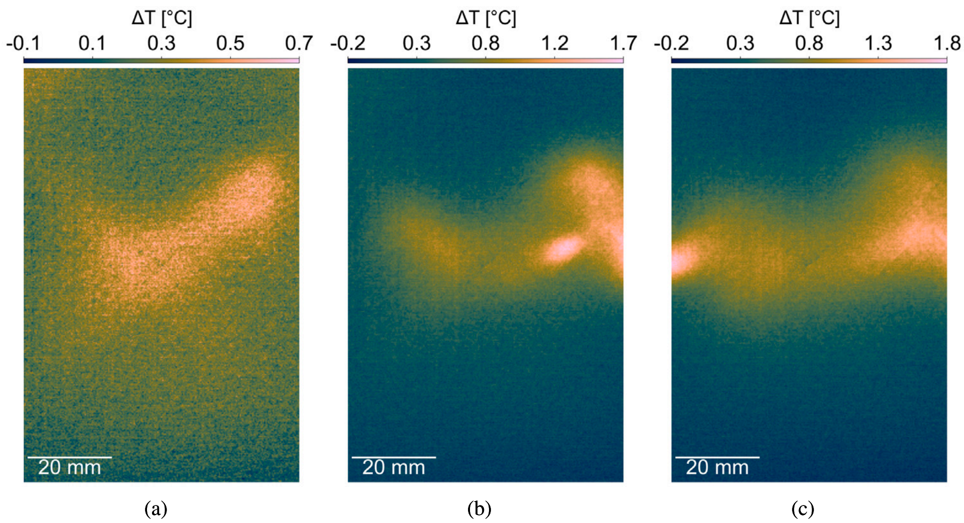

Fig. 16. IR camera pictures of the Taper45-5 specimen obtained approximately (a) 27 kN, (b) 19 kN and (c) 15 kN (after max. force).

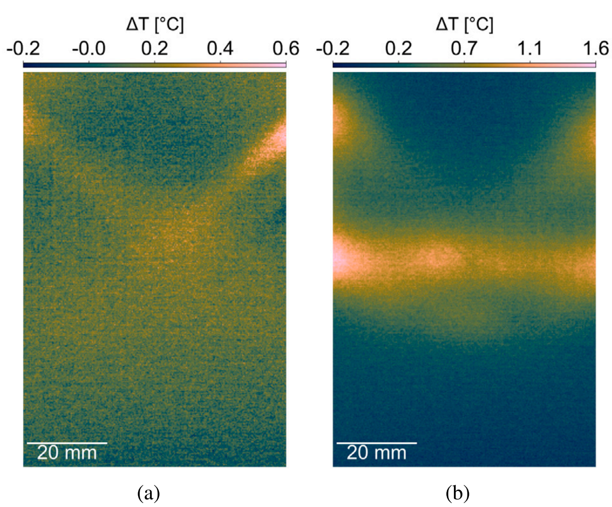

Fig. 17. IR camera pictures of the Taper30-4 specimen obtained approximately (a) 33 kN and (b) 25 kN (after maximum force).

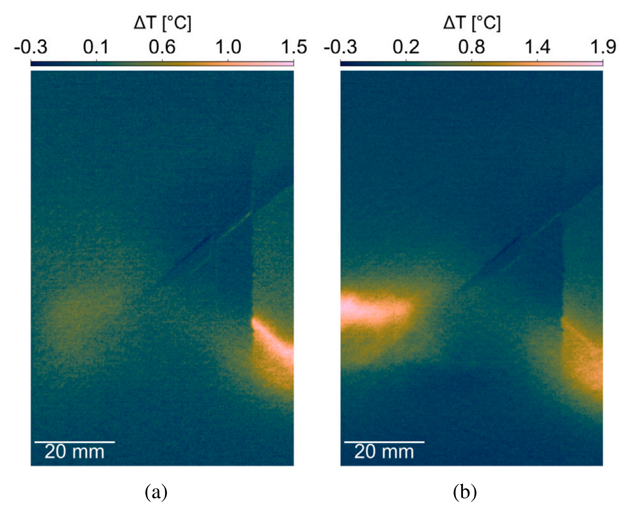

Fig. 18. IR camera pictures of the Taper45-600-5 specimen obtained approximately (a) 20 kN and (b) 13 kN (after maximum force).

cross-section allowed to reduce the extent of the damage in the first place, maintaining the flexural stiffness of the material, in addition, the second moment of area of the specimen was higher too. Unlike the two tapered specimens just discussed, the Taper45-600-5 specimen showed a similar behavior to the flat specimens. From this, it can be concluded that the extensive delamination experienced by this type of specimen due to the low-velocity impact, compromised the flexural stiffness and load-bearing capability, leading to larger out-of-plane displacement.

The Flat45 and Taper45 compression load vs vertical displacement curves have similar behavior (Fig. 7(a) and 7(c)), with a large non-linear part of the curve, despite showing significantly different behavior in terms of out-of-plane displacement, i.e., one showing relatively large displacement while the other shows negligible out-of-plane displacement. The curve in Fig. 20 allows to exclude that the source of non-linearity for the Taper45 specimen is the global buckling, rather, the macroscopic non-linear shear behavior and fibers shearing at high loads. The same conclusion cannot be drawn for the flat specimen, while having fibers aligned along the same direction and being susceptible to the same shear behavior, global buckling significantly contributed to the structural behavior of that set of specimens.

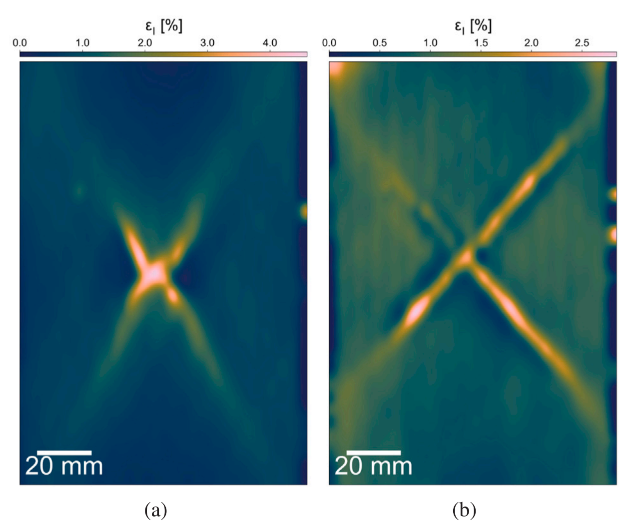

Fig. 19. DIC contour pictures of the major strain component of (a) the Flat30-5 and (b) the Taper45-5 specimens obtained at maximum force).

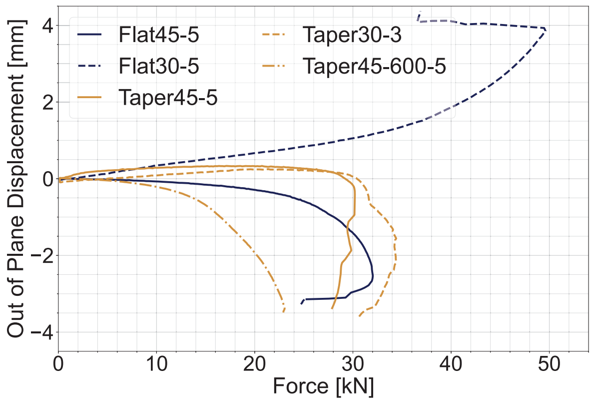

Fig. 20. Out of plane displacement measured by DIC during CAI test of specimens impacted at 33 J.

Table 7
Summary of FEM CAI analyses results and percentage error relative to experimental results.

Specimens		Maximum Force [kN]	Displacement at max. force [mm]
Flat30 FEM	15 J	64.43	1.04
	22 J	65.79	1.01
	33 J	62.74	1.03
Taper45 FEM	15 J	30.65	1.21
	22 J	29.81	1.21
	33 J	28.30	1.10
	40 J	27.51	1.08
Flat30 FEM |Error| [%]	15 J	13.83	11.15
	22 J	10.31	12.52
	33 J	9.26	15.49
Taper45 FEM |Error| [%]	15 J	3.30	204.32
	22 J	1.97	230.12
	33 J	4.82	69.35
	40 J	2.39	80.59

Table 8
Numerical impact stiffness and percentage error relative to experimental results.

Specimens	Flat30	Taper45
Stiffness [kN/mm]	65.64	5.69
|Error| [%]	29.07	16.15

5.6. Finite element model results

It is chosen to model the Flat30 and Taper45 specimens only. The behavior of the Flat30 set aligns better with the indication from the standard, since experimentally it shows almost a linear behavior until the maximum force is reached. The latter instead was considered because the full set is available experimentally. Also, it is not possible to make a FEM comparison of the Taper45 and Taper45-600 specimens because a full material characterization would be required to obtain accurate results. The experimental force versus displacement curves are compared with the FEA results in Figs. 21 and 22. Tables 7 and 8 report the maximum force, displacement at maximum force, stiffness, and percentage error. The percentage error is evaluated as the difference between experimental and FEA results, normalized by the FEA value.

The FEM model of the Flat30 specimens replicates well the force–displacement behavior of the experimental curves, as shown in Fig. 21. The methodology adopted to calibrate the stiffness and strength of the material is effective, replicating the initial stiffness of the specimens, as well as the maximum compressive force and vertical displacement at maximum force. The FEM analyses consistently overestimate these two values maximum by 15%; the overestimation is likely to be the result of the ideal boundary condition of the FEM simulations, as well as the neglecting of the residual deformation of the specimen. After the maximum force is reached, the load drops similarly to what occurs experimentally, however, due to the very low time increment of the analyses after the maximum force and the many elements stiffness degradation, the simulation is interrupted shortly after the maximum load and the force plateau is never reported in the FEM analyses.

In Fig. 22, the maximum force of the tapered specimen resulted from the FEM analyses is within 5% difference; confirming again the validity of the material model adopted and the modeling strategy of the tapered specimen. However, the displacement at maximum force is significantly underestimated, after the previous discussion in Section 5.5 the explanation of this mismatch is associated with the fact that the FEM model does not account for material non-linearities before the failure criteria are met. As a result of the ideal boundary condition and geometry of these FEM models, other factors might contribute to the global non-linear behavior of these tests, such as compliance of the material at the specimen ends at high loads, and underestimated out-of-plane displacement due to perfect initial geometry.

Finally, the damage contour plots showing the damage variables according to Hashin's failure modes are presented in Figs. 23 and 24 for the two different types of models considered in this work. The plots are taken shortly after the maximum force is reached and the force begins to drop (approximately at 50 kN and 25 kN, respectively), to portray better the damage that triggered the failure, as it was assessed in the previous Section being caused by intra-laminar damage. The fiber tension failure mode is not reported because it does not contribute to the specimen failure. For brevity, the results are shown for the CAI simulations performed after the low-velocity impact analyses at 33 J. Since the CAI analyses were carried out accounting for the elements damage resulting from the low-velocity impact analyses that were previously carried out, the contour plots showed in this Section utilize a truncated colorbar at 3/4 of the total color range. The upper bound of the colorbar is used to mark the damage originating from the low-velocity impact.

The fiber compression failure mode barely contributes to the loss of load-bearing capability according to the FEM models, only for the flat specimen model the damaged area increases slightly on the impact side, but it does not affect as relevantly as the other failure modes. This further confirms what has been previously discussed in the previous Sections, failure is triggered by matrix and shear failure along the direction of the fibers, then can lead to other damage mechanisms involving fibers failure, and transversal cracks.

Matrix-governed failure modes cause the failure in the FEM models. Despite a similar type of failure, i.e., elements failed along the directions of the fibers, the loss of loading capability is the result of different mechanisms. For the flat specimen, the matrix tension failure criterion is met, leading to the stiffness loss of elements along the fiber direction; then, as the number of damaged elements increases, the damage variable associated with matrix compression increases slightly near the impact location. The damage predicted by the FEM model represents well the mechanism observed experimentally: the crack propagated from the pre-existing impact damage, leading to fracture along the fiber direction. On the other hand, for the tapered specimens matrix compression criterion causes the failure of the specimen, as highlighted by the series of failed elements. In this case, once these elements have failed due to this criterion, the damage variable associated with matrix tension increases too, contributing to degrading the stiffness along the same direction. Also in this case the fracture along the direction of the fibers is predicted by the FEM models, however, the models do not predict any fracture transversal to the loading direction, unlike what resulted by the IR camera recording during the tests of the tapered specimens. This difference in the contributing mechanisms is associated with the different global displacement behavior. Similarly to the experimental tests, the flat specimen tends to have larger out-of-plane

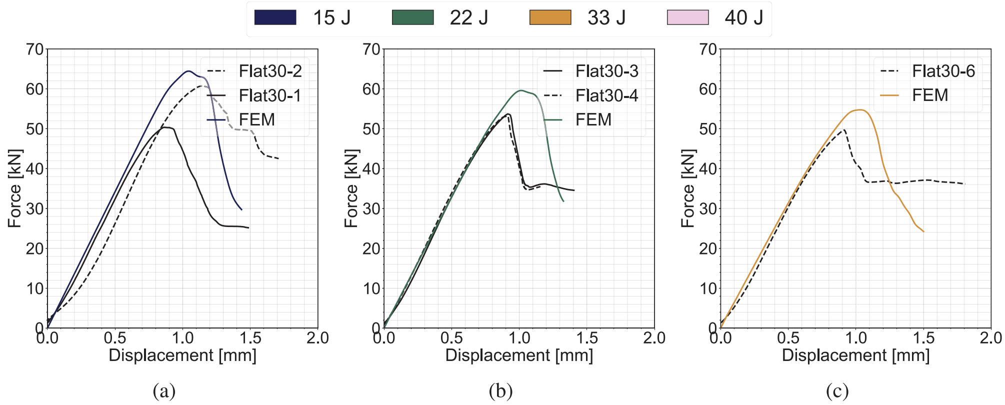

Fig. 21. Numerical and experimental load vs. displacement impact curves of the Flat30 specimens.

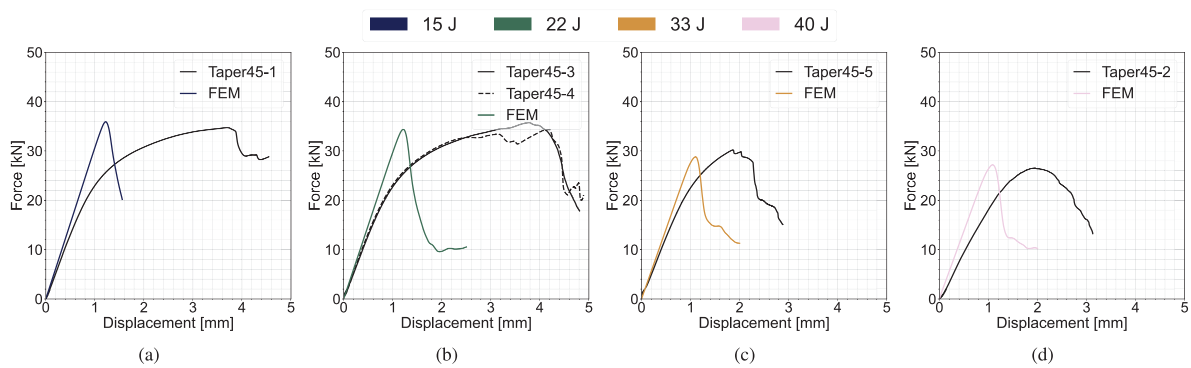

Fig. 22. Numerical and experimental load vs. displacement impact curves of the Taper45 specimens.

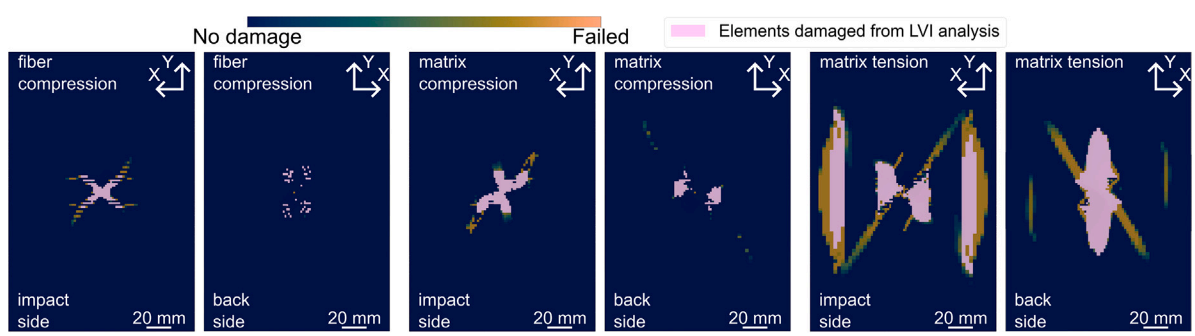

Fig. 23. FEM damage contour images of Flat30 specimen.

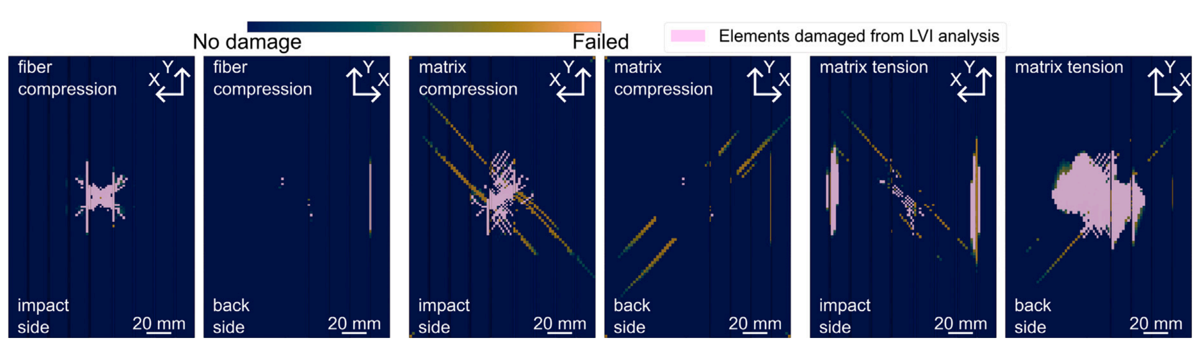

Fig. 24. FEM damage contour images of Taper45 specimen.

displacement, leading to tensile strain, hence matrix tensile damage; while the tapered specimen does not buckle globally, leading to an in-plane compression state of stress that causes matrix compression damage. To conclude, in the CAI analyses the failure is triggered by in-plane failure modes, that are accounted for by Hashin's criteria, the delamination does not affect the maximum force and does not propagate in the early stage of loss of load-bearing capability that is discussed in this Section.

6. Conclusions

Five sets of SD specimens were tested according to the CAI standard testing procedure in this study. The specimens were manufactured then subjected to low velocity impact in a previous work. Two sets of flat specimens were constituted by [± 45°] and [± 30°] NCFs, respectively, then two sets of tapered specimens with the same NCFs and a fifth set with [± 45°] NCFs with a different areal density. The tapered specimens were manufactured using the card-sliding technique, consisting of offsetting groups of plies to achieve a tapered cross-section. The experimental tests were carried out according to the ASTM testing procedure and employed an IR camera to record the thermal transient and a DIC system to capture the displacement on the back and impact side of the specimen, respectively. In addition, numerical simulations were performed and compared with the experimental observations to investigate damage mechanisms.

The specimens manufactured with [± 45°] NCFs showed significant non-linear behavior because of global instability and non-linear material behavior, while the specimens manufactured with [± 30°] fabrics presented a more linear behavior in the force–displacement curves, as well as larger maximum force and lower maximum displacement, especially comparing to the Flat coupons. The damage and failure modes of the specimens were first discussed with optical camera and cross-section cut pictures of the tested specimens, then the analysis was further detailed by the results of the IR camera and the DIC system. Flat specimens failure was characterized by fracture running along the fiber orientation, originating from the area of the specimens damaged by the impact and caused by the compression and shear state of stress generated in the laminate. The Tapered specimens presented similar failure modes and it was shown that the same failure mode causes the loss of load bearing capability, however, other features appear in these specimens, such crack propagating along the transverse direction with respect to the loading direction. Thermographic and DIC analysis provided important insights, highlighting damage mechanisms and global behavior of the specimen. Finite element modeling provided additional insights into the experimental findings, effectively replicating damage patterns, despite limited accuracy of the force–displacement behavior.

This research offers new insights into damage tolerance and failure mechanism of SD composite, examining specimens made using the innovative SD (or DD) stacking sequence and card-sliding tapering technique. The three sets of tapered specimens investigated provided valuable information on damage mechanisms, possibly contributing to apply in the future these novel stacking sequence and tapering strategy, to optimize composite structures weight and performance. Future studies will explore the damage tolerance of specimens manufactured with DD stacking sequence too, as well as perform full characterization of the NCFs to address the shortcomings of the material data available. Another critical aspect to consider is the tapering strategy, which can affect the resin pockets and the structural behavior in both low-velocity impacts and CAI. These strategies to refine the card-sliding process could potentially mitigate delamination risks and encourage intra-laminar failure, ultimately improving the durability and damage tolerance of composite materials.

CRediT authorship contribution statement

Alessandro Vescovini: Writing – original draft, Validation, Methodology, Investigation, Conceptualization. **Carina Xiaochen Li:** Writing – review & editing, Methodology, Investigation. **Bo Cheng Jin:** Writing – review & editing, Supervision, Methodology, Funding acquisition, Conceptualization. **Andrea Manes:** Writing – review & editing, Supervision, Funding acquisition.

Declaration of competing interest

The authors declare that they have no known competing financial interests or personal relationships that could have appeared to influence the work reported in this paper.

Data availability

Data will be made available on request.

References

[1] C. Kassapoglou, Modeling the Effect of Damage in Composite Structures: Simplified Approaches, John Wiley & Sons, Ltd, 2015, pp. 105–170.
[2] S. Abrate, Impact on Composite Structures, Cambridge University Press, 1998.
[3] A. Tropis, M. Thomas, J.L. Bounie, P. Lafon, Certification of the composite outer wing of the ATR72, Proc. Inst. Mech. Eng. Part G: J. Aerosp. Eng. 209 (4) (1995) 327–339.
[4] M.R. Wisnom, The role of delamination in failure of fibre-reinforced composites, Philos. Trans. R. Soc. A: Math. Phys. Eng. Sci. 370 (1965) (2012) 1850–1870.
[5] Xin Wang, Jun Huang, Riming Tan, Yuru Su, Zhidong Guan, Xia Guo, Experimental investigation on damage mechanisms and buckling behaviors of thin composite laminates in compression after impact, Compos. Struct. 256 (2021) 113122.
[6] Han Yin, Lorenzo Iannucci, An experimental and finite element investigation of Compression-After-Impact (CAI) behaviour of biaxial carbon fibre Non-Crimp-Fabric (NCF) based composites, Compos. Struct. 281 (2022) 115057.
[7] Stephen W. Tsai, José Daniel D. Melo, Composite Materials: Design and Testing, Composites Design Group, 2015.
[8] S.W. Tsai, N. Sharma, A. Arteiro, S. Roy, B. Rainsberger, Composite double-double and grid/skin structures-low weight/low cost design and manufacturing, 2019, Composites Design Group, Stanford.
[9] Sachin Shrivastava, Naresh Sharma, Stephen W. Tsai, P.M. Mohite, D and DD-drop layup optimization of aircraft wing panels under multi-load case design environment, Compos. Struct. 248 (2020) 112518.
[10] Bruno Vermes, Stephen W. Tsai, Thierry Massard, George S. Springer, Tibor Czigany, Design of laminates by a novel "double–double" layup, Thin-Walled Struct. 165 (2021) 107954.
[11] Stephen W. Tsai, Double–double: new family of composite laminates, AIAA J. 59 (11) (2021) 4293–4305.
[12] Erik Kappel, Double–Double laminates for aerospace applications—Finding best laminates for given load sets, Compos. Part C: Open Access 8 (2022) 100244.
[13] Erik Kappel, Buckling of simply-supported rectangular Double–Double laminates, Compos. Part C: Open Access 11 (2023) 100364.
[14] Erik Kappel, On the Double-Double laminate buckling optimum for the 18-panel 'Horse-Shoe' reference case, J. Compos. Sci. 8 (2) (2024).
[15] Alessandro Vescovini, Carina Xiaochen Li, Javier Paz Mendez, Bo Cheng Jin, Andrea Manes, Chiara Bisagni, Post-buckling behavior and collapse of Double-Double composite single stringer specimens, Compos. Struct. 327 (2024) 117699.
[16] Erik Kappel, Yannick Boose, Mirko Mißbach, A CAI study on transition zones of conventional and Double-Double laminates, Compos. Part C: Open Access 14 (2024) 100450.
[17] Hakim Abdulhamid, Christophe Bouvet, Laurent Michel, Jacky Aboissière, Clément Minot, Experimental study of compression after impact of asymmetrically tapered composite laminate, Compos. Struct. 149 (2016) 292–303.
[18] Nicola Tessitore, Aniello Riccio, A novel FEM model for biaxial non-crimp fabric composite materials under tension, Comput. Struct. 84 (19–20) (2006) 1200–1207.
[19] A. Arteiro, G. Catalanotti, J. Xavier, P.P. Camanho, Notched response of non-crimp fabric thin-ply laminates, Compos. Sci. Technol. 79 (2013) 97–114.
[20] A. Arteiro, G. Catalanotti, J. Xavier, P.P. Camanho, Large damage capability of non-crimp fabric thin-ply laminates, Compos. Part A: Appl. Sci. Manuf. 63 (2014) 110–122.
[21] Alessandro Vescovini, Carina Xiaochen Li, Cecilia Malverti, Bo Cheng Jin, Andrea Manes, Low-velocity impact behavior of flat and tapered Single–Double composites specimens, Compos. Struct. 355 (2025) 118823.
[22] Chomarat, C-PLY™SP BX45 100 C3,4 12K HS, 2014.
[23] Chomarat, C-PLY™SP BX30 100 C3,4 12K HS, 2015.
[24] Chomarat, C-PLY™SP BX45 600 C3,4 50K HS, 2014.
[25] ProSet, Technical Data, INF-114 INF-212, Infusion Epoxy, 2013.
[26] Stephen W. Tsai, Double–Double: New family of composite laminates, AIAA J. 59 (11) (2021) 4293–4305.
[27] ASTM D7136/D7136M - 15 standard test method for measuring the damage resistance of a fiber-reinforced polymer matrix composite to a drop-weight impact event, 2015.

[28] ASTM D7137/D7137M - 17 standard test method for compressive residual strength properties of damaged polymer matrix composite plates, 2017.
[29] ABAQUS/Standard User's Manual, Version 2023, Dassault Systemes Simulia Corp, United States, 2023.
[30] Z. Hashin, Failure criteria for unidirectional fiber composites, J. Appl. Mech. 47 (2) (1980) 329–334.
[31] M.L. Benzeggagh, M. Kenane, Measurement of mixed-mode delamination fracture toughness of unidirectional glass/epoxy composites with mixed-mode bending apparatus, Compos. Sci. Technol. 56 (4) (1996) 439–449.
[32] A. Arteiro, P.J. Gray, P.P. Camanho, Simulation of edge impact and compression after edge impact in CFRP laminates, Compos. Struct. 240 (2020) 112018.
[33] Albertino José Castanho Arteiro, Technology Development and Structural Mechanics of Composites Built of Spread Tow Thin-Ply Technology, FEUP, 2012.
[34] Robin Olsson, Analytical prediction of large mass impact damage in composite laminates, Compos. Part A: Appl. Sci. Manuf. 32 (9) (2001) 1207–1215.
[35] Robin Olsson, Analytical prediction of damage due to large mass impact on thin ply composites, Compos. Part A: Appl. Sci. Manuf. 72 (2015) 184–191.
[36] Fabio Crameri, Grace E. Shephard, Philip J. Heron, The misuse of colour in science communication, Nat. Commun. 11 (5444) (2020).
[37] Mehmet Aktaş, Ramazan Karakuzu, Yusuf Arman, Compression-after impact behavior of laminated composite plates subjected to low velocity impact in high temperatures, Compos. Struct. 89 (1) (2009) 77–82.
[38] S.T. Pinho, L. Iannucci, P. Robinson, Physically based failure models and criteria for laminated fibre-reinforced composites with emphasis on fibre kinking. Part II: FE implementation, Compos. Part A: Appl. Sci. Manuf. 37 (5) (2006) 766–777.